

The Distance and Peculiar Velocity of the Norma cluster (ACO 3627) using the Near-Infrared J and K_s -band Fundamental Plane Relations.

T. MUTABAZI^{1,2}

¹*Department of Physics, Mbarara University of Science and Technology, P.O. Box 1410, Mbarara, Uganda*

²*Astrophysics, Cosmology and Gravity Centre (ACGC), Astronomy Department, University of Cape Town, Private Bag X3, Rondebosch, 7701, South Africa*

ABSTRACT

We report distance measurements for the Norma cluster based on the near-infrared J - and K_s -band Fundamental Plane (FP) relations. Our simultaneous J and K_s -band photometry analyses were performed using 31 early-type galaxies in the nearby Norma cluster obtained using the 1.4 m InfraRed Survey Facility (IRSF) at the South African Astronomical Observatory. Our final K_s -band FP sample consists of 41 early-type galaxies from the Norma cluster observed using the IRSF and the New Technology Telescope (NTT) at the European Southern Observatory. This is the largest cluster sample used for peculiar velocity studies in the Great Attractor region to date. From the K_s -band FP, we find a distance to the Norma cluster of 4915 ± 121 km s⁻¹. The implied peculiar velocity for Norma is 44 ± 151 km s⁻¹ which further supports a small peculiar velocity for the Norma cluster.

1. INTRODUCTION

While the Norma cluster (ACO 3627) was identified and catalogued by [Abell et al. \(1989\)](#), this cluster's massive nature and dynamical role in the Great Attractor (GA) region were not realised until the mid 1990s ([Kraan-Korteweg et al. 1996](#); [Boehringer et al. 1996](#); [Tamura et al. 1998](#)). The Norma cluster has since been identified by [Woudt et al. \(2008\)](#) as the richest cluster in the GA region. Studies in this region are affected by high levels of Galactic extinction and star-crowding due to its location at low Galactic latitudes. Some large scale structures are therefore expected to still remain hidden within this zone of obscuration ([Sorice et al. 2017](#); [Courtois et al. 2019](#)) as evidenced by the recent discovery of the Vela supercluster ([Kraan-Korteweg et al. 2017](#)). Currently, there is significant improvement in our understanding of the large scale structures residing in the zone of avoidance through observations at near-infrared wavelengths where the effect of Galactic extinction significantly reduces (e.g. [Macri et al. 2019](#)). Using telescopes with superior resolution such as the IRSF and NTT minimises the effects of high stellar density (star-crowding) in this region (see e.g. [Said et al. 2016a](#)). In addition, 21-cm radio observations ([Said et al. 2016b](#); [Staveley-Smith et al. 2016](#); [Kraan-Korteweg et al. 2018](#); [Schroder et al. 2019](#)) have revealed the abundance and massive nature of galaxies in this region. Such HI observations are not affected by Galactic ex-

inction but may suffer from radio contamination from neighbouring radio sources.

The Local Group has a well known peculiar velocity ($v_{LG} = 627 \pm 22$ km s⁻¹) with respect to the CMB rest frame in the direction $\ell = 276^\circ \pm 3^\circ$, $b = 30^\circ \pm 3^\circ$ ([Kogut et al. 1993](#)) — which is in the direction of Shapley ([Shapley 1930](#); [Raychaudhury 1989](#); [Scaramella et al. 1989](#)) and Vela ([Kraan-Korteweg et al. 2017](#)) superclusters. Despite more than two decades of study, the fractional contribution of the GA and Shapley supercluster on the Local Group's peculiar velocity remains a topic of debate (see e.g. [Smith et al. 2000](#); [Lucey et al. 2005](#); [Erdoğdu et al. 2006](#); [Kocevski & Ebeling 2006](#); [Lavaux et al. 2010](#); [Carrick et al. 2015](#)).

In the analysis by [Lavaux et al. \(2010\)](#), they recovered the majority of the amplitude of the Local Group's peculiar velocity within $120h^{-1}$ Mpc but the direction of motion did not agree with the expected direction of the CMB dipole — they suggested convergence may lie as far as $200h^{-1}$ Mpc which is supported by recent measurements using the 2M++ sample ([Carrick et al. 2015](#)). While some authors found small contributions from the Shapley Supercluster (e.g., [Bardelli et al. 2000](#); [Bolejko & Hellaby 2008](#)), significant contributions from distant structures have been supported by e.g. [Kocevski & Ebeling \(2006\)](#); [Springob et al. \(2014, 2016\)](#); [Hoffman et al. \(2017\)](#); [Qin et al. \(2018\)](#); [Tully et al. \(2019\)](#); [Said et al. \(2020\)](#).

Although the zone of avoidance or zone of obscuration has received less attention, structures hidden within or behind this region may play a role in the general flow and may significantly contribute to the Local Group's motion. An example is the recent discovery of an extended

supercluster of galaxies at $cz \sim 18000 \text{ km s}^{-1}$, located at Galactic longitudes and latitudes $(\ell, b) \sim (272^\circ, 0^\circ)$ (Kraan-Korteweg et al. 2017). This previously hidden Vela supercluster was later kinematically confirmed by Courtois et al. (2019). Using Cosmicflows-3 which is a compilation of distances for ~ 18000 galaxies (Tully et al. 2016), Courtois et al. (2017) found dominant features (repulsive and attractive), the major basin of attraction corresponding to an extension of the Shapley supercluster. This is in agreement with the previous findings based on the 6dF Galaxy Peculiar Velocity Survey where positive line-of-sight peculiar velocities were estimated, suggesting substantial mass overdensities originating at distances further away than the Great Attractor (Springob et al. 2016). There is currently increasing support for flow towards more distant structures such as Vela and Shapley superclusters (see e.g. Kocevski & Ebeling 2006; Springob et al. 2014; Staveley-Smith et al. 2016; Hoffman et al. 2017; Tully et al. 2019).

Located at $(\ell, b, v_{\text{hel}}) = (325^\circ, -7^\circ, 4871 \pm 54 \text{ km s}^{-1})$ — see for example, Woudt et al. (2008), the Norma cluster lies close to the anticipated centre of the GA (Kolatt et al. 1995). As such, a reliable estimate of the redshift-independent distance (and hence the peculiar velocity) of the Norma cluster is crucial to understanding the GA flow. Our previous measurements (Mutabazi et al. 2014) show the Norma cluster to have a small peculiar velocity, consistent with zero (i.e. $v_{\text{pec}} = -72 \pm 170 \text{ km s}^{-1}$).

In order to improve the Fundamental Plane (FP) distance of Norma, we have made new J and K_s -band photometric measurements using near-infrared (NIR) images from the 1.4 m Japanese InfraRed Survey Facility (IRSF) at the Sutherland site of the South African Astronomical Observatory. We improve on our previous results by studying the effect of Galactic extinction using the $J - K_s$ colour for these new data. In addition, we have extended/improved our previous K_s -band FP analysis from $N = 31$ to a total sample of 41 Norma cluster early-type galaxies (ETGs) selected from within $\frac{2}{3}R_A$ where R_A is the Norma cluster's Abell radius.

In this paper, we therefore present (1) distance and peculiar velocity for the Norma cluster using the J and K_s -band FP (Djorgovski & Davis 1987; Dressler et al. 1987) analysis for 31 ETGs whose NIR images were obtained using IRSF (2) a combined K_s -band FP analysis for a total of 41 ETGs whose NIR images were obtained using the IRSF and NTT telescopes (see Mutabazi et al. 2014, for telescope details). For ETGs that were observed using both the IRSF and NTT, the NTT data was given priority due to its superior resolution and good seeing conditions. Note however that both datasets have high quality, highly resolved data (NTT and IRSF have pixel scales of 0.29 and 0.45 arcsec per pixel, respectively) which are very well suited for this study.

This paper is structured as follows: Sample selection and observations for our FP sample is discussed in §2 while the photometric data and analysis are presented and discussed in §3. A re-calibration of the NIR reddening maps is presented in §3.4. In §4, we present the measured zero-point offset using the FP relation. The distance and peculiar velocity measurements are presented in §5. The discussion and conclusions of our findings are presented under §6.

Unless stated, we have adopted standard cosmology with $\Omega_m = 0.27$, $\Omega_\Lambda = 0.73$ and $H_0 = 70.5 \text{ km s}^{-1} \text{ Mpc}^{-1}$ (Hinshaw et al. 2009). While measuring the distance of the Norma cluster relative to the Coma cluster, we used $z_{\text{CMB}} = 0.02400 \pm 0.00016$ for the Coma cluster (Hudson et al. 2004).

2. OBSERVATIONS AND DATA REDUCTION

2.1. Sample selection

The ETGs used in the Norma cluster sample were such that (1) $2096 \text{ km s}^{-1} < v_{\text{hel}} < 7646 \text{ km s}^{-1}$ where v_{hel} is the galaxy's heliocentric velocity (2) lie within $\frac{2}{3}$ of the Abell radius, and (3) we had successfully measured the central velocity dispersion using the 2dF spectrograph. The above selection criteria resulted in a total of 31 ETGs with J and K_s -band images from the IRSF telescope. Ten of these 31 ETGs with IRSF images are unique to the IRSF while 21 ETGs have NIR images from both the IRSF and NTT.

For the Coma cluster sample, galaxies selected were those typed as E or E/S0 or S0 by Dressler (1980), were identified and confirmed as Coma cluster members based on their redshifts, and had a central velocity dispersion in the Sloan Digital Sky Survey Data Release 8 (Aihara et al. 2011). In addition, only those which we successfully measured the FP photometry parameters from the 2MASS Atlas images were selected. This resulted in a Coma cluster sample of 121 ETGs.

2.2. Observations with the IRSF

The IRSF telescope is equipped with SIRIUS, a three-colour band camera with three 1024×1024 pixels HgCdTe infrared detectors and is capable of simultaneous imaging in the J , H and K_s passbands (Nagashima et al. 1999). Our IRSF observations were carried out using a total integration time of 600 s split over 20 short exposures of 30 s each. Standard NIR data reduction procedures (such as dark subtraction, flat-fielding, sky subtraction) were applied before combining the 20 dither frames into one science image. Note that both the NTT and IRSF telescopes are suitable for the high stellar density GA region since they are equipped with the SOFI and SIRIUS imaging instruments which have a low pixel scale, that is, 0.29 arcsec per pixel and 0.45 arcsec per pixel, respectively. It is also important to note that the combined K_s -band data (IRSF+NTT) is the largest cluster sam-

ple ($N = 41$) used for peculiar velocity studies in the GA region to date.

To ensure that all our photometry data sets are on the same photometric system, the astrometric and photometric calibrations were performed using the 2MASS Point Source Catalogue (Skrutskie et al. 2006). During the photometric calibration process, we applied a small correction due to the slight difference between the 2MASS, NTT and IRSF filters (see e.g., Carpenter 2001).

3. PHOTOMETRY DATA ANALYSIS

In order to apply the FP relation, measurements of the effective radii and mean effective surface brightnesses are required. These were measured through galaxy surface brightness profile fitting.

3.1. Galaxy surface brightness profile fitting

For accurate photometry, stars in each galaxy field were subtracted after which a reliable estimate of the sky background was calculated using an annulus as described in Mutabazi et al. (2014). We performed the photometric analysis (for both Norma and Coma galaxies) using the ELLIPSE (Jedrzejewski 1987) task in IRAF. The resulting surface brightness profiles were fitted using a combination of two Sérsic functions. The best fit was extrapolated to infinity so as to estimate the total extrapolated magnitude. The effective radius was then measured through interpolation. To correct for the seeing (PSF) effects, the GALFIT algorithm (Peng et al. 2010) was used with and without a PSF convolution. Figure 1 is an example of the fitted profiles for WKK 6250, one of the Norma cluster’s galaxies from the IRSF data. The top panel is the J -band while the bottom panel represents the K_s -band. The fit data were restricted to within the radius ranging from twice the seeing to where the galaxy flux averages to $1\sigma_s$ above the sky background. These are represented by the two small magenta arrows. The black solid line is the best fit which is a combination of the two Sérsic component fits represented by the red and blue dashed lines. The inset shows the residuals.

3.2. Photometry comparisons

As a photometric reliability check, we took advantage of the high quality, high resolution images provided by both the NTT (pixel scale of 0.29 arcsec per pixel) and IRSF (pixel scale of 0.45 arcsec per pixel) telescopes. We compared the K_s -band total extrapolated magnitudes for an overlapping sample of 21 ETGs (ETGs which are common to both the IRSF and NTT data). The comparison shows excellent agreement as seen in Figure 2, i.e., an average difference in total extrapolated magnitudes of 0.000 ± 0.021 mag although with a relatively large scatter of 0.095 mag. This scatter is dominated by WKK 6204 with a very uncertain

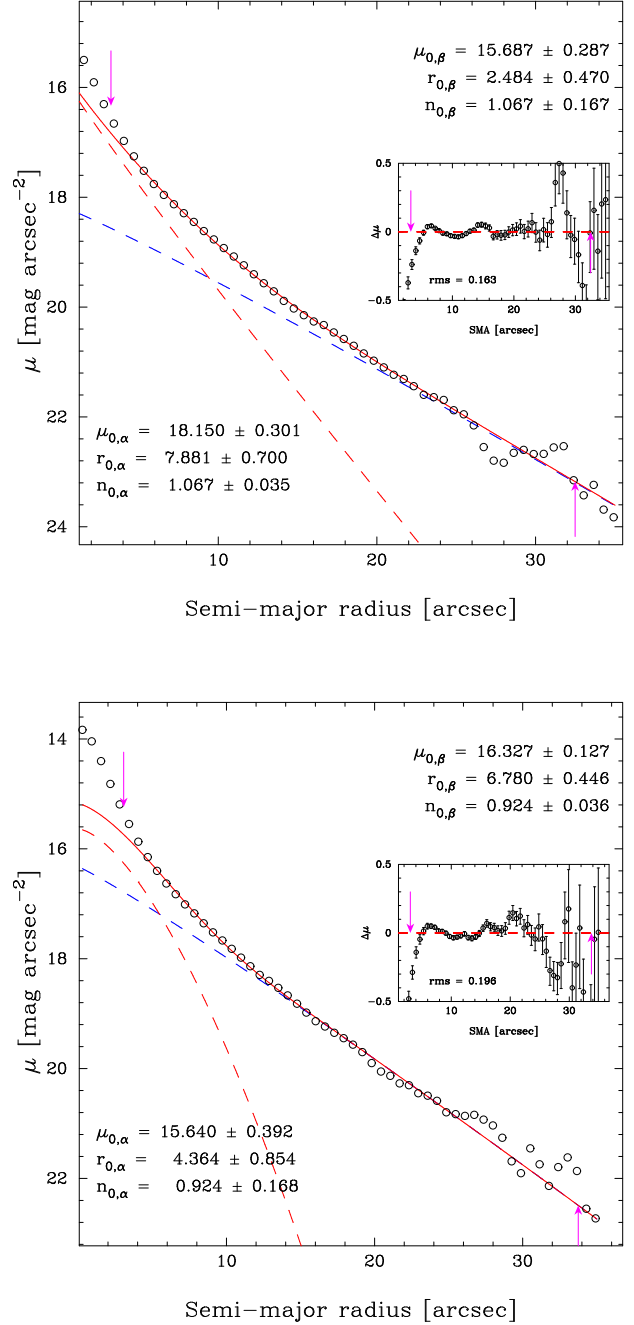


Figure 1. Double Sérsic component fits to the galaxy surface brightness profile for WKK 6250 in the J (top panel) and K_s -band (bottom panel). The red and blue dashed lines represent the individual Sérsic components while the red solid line represents the combined fit (best fit to the galaxy surface brightness profile). The small magenta arrows represent twice the seeing (FWHM) and the radius where the galaxy surface brightness reaches the sky background noise level. Only the data within the range indicated by these two magenta arrows were used to fit the galaxy surface brightness profile.

IRSF K_s -band magnitude. When this galaxy (WKK 6204) is excluded from the comparison between the IRSF and NTT

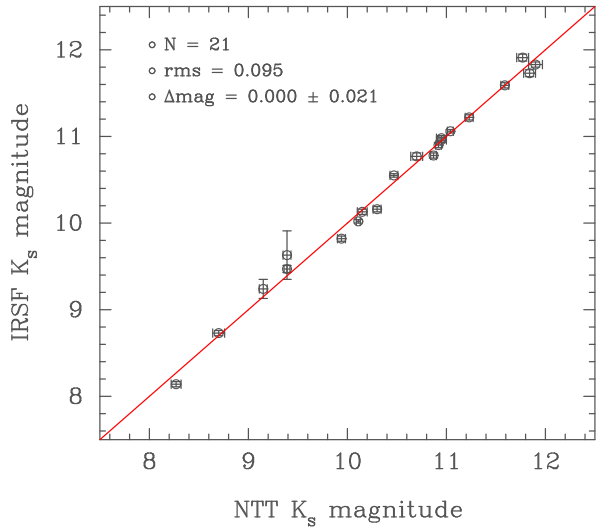


Figure 2. Comparison between the total extrapolated magnitudes for the 21 ETGs observed using both the NTT and IRSF telescopes. The red solid line shows a one-to-one relation. Both the average magnitude and rms were computed based on this line.

magnitudes, the mean difference is 0.0125 ± 0.0180 mag and the rms reduces from 0.095 to 0.080. However, the effect on the IRSF K_s -band Fundamental Plane analysis is not very significant – the rms from the FP fit decreases slightly from 0.0778 to 0.0776 when WKK 6204 is included and excluded, respectively. The source of the large uncertainty on the IRSF K_s -band magnitude for this galaxy (WKK 6204) is not very clear since the error/uncertainty in the IRSF J -band magnitude is significantly lower than the IRSF K_s -band magnitude for this same galaxy (0.07 mag in J and 0.28 mag in K_s -band). It should however be noted that there were sky gradients in the observed field for this galaxy using IRSF as compared to NTT possibly due to a superior resolution and better seeing conditions associated with NTT. These sky gradients are most likely due to a nearby bright galaxy in the field of WKK 6204. Therefore, the large uncertainty on the IRSF magnitude for WKK 6204 could be due to the error associated with the measured sky background in the K_s -band as a result of this nearby galaxy. The effect may be more pronounced in the K_s image since the nearby galaxy is brighter in the K_s than in the J -band. Note that the central velocity dispersions used in our analysis were taken from the Sloan Digital Sky Survey Data Release 8 (Aihara et al. 2011) for the Coma cluster sample. For the Norma cluster sample, data using the fibre spectroscopy on the 2dF facility (Lewis et al. 2002) on the 3.9 m Anglo-Australian Telescope were used.

3.3. Coma cluster sample – Photometric analysis

For the Coma cluster, 2MASS Atlas images were used in the photometric analysis. For photometric quality check, we have compared our measurements and the 2MASS XSC for the 121 Coma ETGs.

The mean differences (2MASS – This work) between our measured total extrapolated magnitudes and the values taken from the 2MASS XSC (Skrutskie et al. 2006) are -0.003 ± 0.014 mag and -0.015 ± 0.009 mag in the J and K_s -band, respectively. The photometric results and the corrected FP variables for the Coma sample ($N = 121$) are presented in Table 4.

3.4. Galactic extinction: re-calibration using NIR colours

As Norma is at Galactic latitude, $b = -7$, the Galactic extinction is relatively large. Note that for the Coma cluster, the effect of Galactic extinction is very small, i.e., ~ 0.007 mag and 0.003 mag in the J and K_s -band, respectively. The Schlegel et al. (1998) NIR reddening maps have been found to over-estimate the Galactic extinction especially at low Galactic latitudes (Bonifacio et al. 2000; Yasuda et al. 2007; Schröder et al. 2007; Schlafly & Finkbeiner 2011). A re-calibration of the NIR reddening maps based on the $J - K_s$ colour for the Norma and Coma cluster ETGs used in our FP analysis is presented here. This closely follows the re-calibration by Schröder et al. (2007).

The extinction in the J and K_s bands, assuming the Fitzpatrick (1999) reddening law, with $R_v = 3.1$ is given by

$$A_J = 0.937E(B - V), \quad A_{K_s} = 0.382E(B - V), \quad (1)$$

where $E(B - V)$ is the colour excess or selective extinction. The redshift (k -correction) and extinction-corrected ($J - K_s$) colour is given by

$$(J - K_s)^o = (J - K_s) - 0.555E(B - V) + 4.0z; \quad (2)$$

where, $(J - K_s)$ is the measured NIR colour with no corrections applied while $(J - K_s)^o$ is the NIR colour, corrected for both redshift (k -correction, see §3.5: Equation 15) and Galactic extinction effects. The colour excess, $E(B - V)$ values, were obtained using the DIRBE/IRAS reddening maps (Schlegel et al. 1998). Figure 3 shows the least-squares fit to the Norma sample (top panel) and Coma sample (bottom panel). The J and K_s aperture magnitudes were measured using aperture radii of 5 arcsec. The best fit which is represented by the red dashed line is

$$\text{Norma: } (J - K_s)^o = -0.283 \pm 0.087A_{K_s} + 0.984 \pm 0.037, \quad (3)$$

$$\text{Coma: } (J - K_s)^o = -0.096 \pm 0.056A_{K_s} + 1.050 \pm 0.067 \quad (4)$$

Equations 3 and 4 can be expressed in the form

$$(J - K_s)^o = aA_{K_s} + b; \quad (5)$$

where A_{K_s} is the extinction in the K_s -band which is given by Equation 1, a and b are fit parameters which were measured through simple least-squares regression.

The reddening law for the DIRBE/IRAS reddening maps (Schlegel et al. 1998) following the derivation in

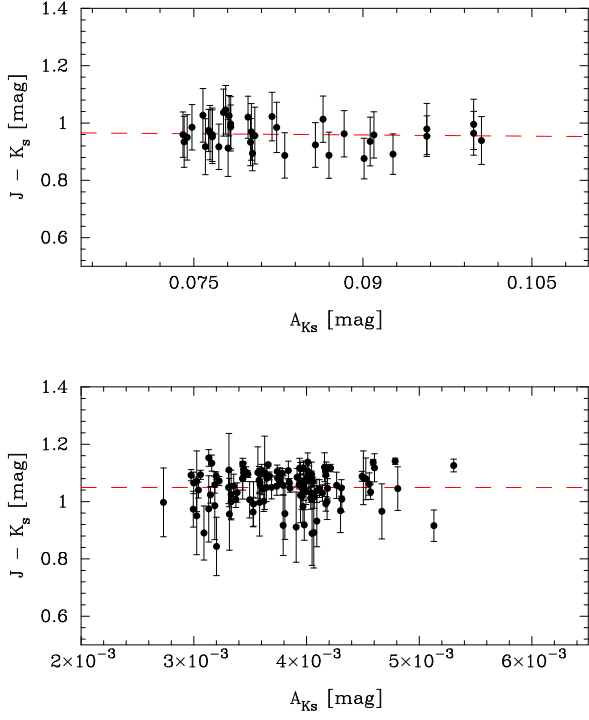


Figure 3. Measuring the extinction correction factor using the $(J - K_s)$ colour for the Norma (top panel) and the Coma (bottom panel) samples. The y-axis is the $(J - K_s)$ colour which has been corrected for both Galactic extinction and redshift effects.

Schröder et al. (2007) can be written as:

$$J - K_s = (J - K_s)^o + \left[\frac{E(J - K_s)}{A_{K_s}} \right] A_{K_s} \quad (6)$$

For the true extinction-corrected colour, $(\widetilde{J - K_s})^o$, and true K_s -band extinction, \tilde{A}_{K_s} , we have

$$J - K_s = (\widetilde{J - K_s})^o + \left[\frac{E(J - K_s)}{A_{K_s}} \right] \tilde{A}_{K_s}. \quad (7)$$

Combining Equations 5 and 6 yields

$$J - K_s = aA_{K_s} + b + \left[\frac{E(J - K_s)}{A_{K_s}} \right] A_{K_s}. \quad (8)$$

Equating Equations 7 and 8 leads to

$$(\widetilde{J - K_s})^o = aA_{K_s} + b + (A_{K_s} - \tilde{A}_{K_s}) \left(\frac{E(J - K_s)}{A_{K_s}} \right). \quad (9)$$

The trend in Equations 3 and 4 implies a multiplicative factor, f , between the applied and true extinction, that is,

$$\tilde{A}_{K_s} = fA_{K_s}. \quad (10)$$

Substituting Equation 10 into 9 results in

$$(\widetilde{J - K_s})^o = a + \left[(1 - f) \frac{E(J - K_s)}{A_{K_s}} \right] A_{K_s} + b. \quad (11)$$

Note that the true colour, $(\widetilde{J - K_s})^o$, is independent of extinction, A_{K_s} . This implies that

$$(1 - f) \frac{E(J - K_s)}{A_{K_s}} = 0. \quad (12)$$

Equation 12 implies that

$$f = 1 + a \left[\frac{E(J - K_s)}{A_{K_s}} \right]^{-1}. \quad (13)$$

From the measured slope (Equations 3 and 4) and the selective extinction given by Equation 1, the extinction correction factors computed from Equation 13 are 0.81 ± 0.06 and 0.93 ± 0.05 for the Norma and Coma samples, respectively. The challenge in our calibration is that, our sample covers a very small area on the sky and hence a very small range of extinction values (see the top and bottom panels of Figure 3). It is however worth the effort given our high quality (high resolution) photometric data. After applying these extinction correction factors (0.81 for Norma and 0.93 for Coma ETGs), the mean differences between the Schlafly & Finkbeiner (2011) K_s -band extinction and our values are relatively small, that is, 0.0081 mag (rms = 0.0008 mag) and 0.0003 mag (rms = 0.000045 mag) for the Norma and Coma ETGs, respectively. The extinction correction factor of 0.81 ± 0.06 implies a range of 0.75–0.87 which translates into a difference of $\sim 43 \text{ km s}^{-1}$ in Norma's distance.

3.5. Corrected effective surface brightnesses

The mean effective surface brightness ($\langle \mu_e \rangle$) was computed using:

$$\langle \mu_e \rangle = m_{\text{tot}} + 2.5 \log(2\pi r_e^2) - A_\lambda + k_\lambda - 10 \log(1 + z), \quad (14)$$

where m_{tot} is the total extrapolated magnitude corrected for the star-subtraction and sky background effects. A_λ is the Galactic extinction, k_λ is the k -correction, and $10 \log(1 + z)$ is a cosmological dimming correction term (λ denotes the filter/band – i.e., J , and K_s). The effective radii for both the Norma and Coma cluster ETGs were determined by measuring the radius of a circle containing half the total flux. These were thereafter corrected for seeing effects (measured using GALFIT). The applied k -correction was adopted from Glass (1999), i.e.,

$$k_J = 0.7z, \quad k_{K_s} = 3.3z. \quad (15)$$

We have compared our adopted k -corrections with those of Chilingarian et al. (2010). The mean differences (for the K_s -band) are 0.022 mag (rms = 0.004 mag) and 0.039 mag (rms = 0.005 mag) for the Norma and Coma samples, respectively. Using the Chilingarian et al. k -correction values lowers the distance of the Norma cluster by $\sim 67 \text{ km s}^{-1}$.

Table 1 shows the results for the Norma cluster sample where the final fully corrected FP variables (r_e , $\langle\mu_e\rangle$, and $\log\sigma$) are presented (also see Table 4 for the Coma sample). Note that for the Norma cluster sample, m_{tot} was first corrected for star-subtraction effects (which are -0.0143 and -0.0135 mag in the J and K_s -band, respectively). An additional small correction (-0.011 and -0.008 mag in the J and K_s -band, respectively) due to sky background variation was also applied. This correction was measured (in our analysis) through simulations conducted using our IRSF J and K_s -band images.

4. NORMA DISTANCE: FP ZERO-POINT OFFSET

4.1. Construction of the Fundamental Plane data sets

The FP relation requires the effective radius, r_e , mean effective surface brightness, $\langle\mu_e\rangle$, and the central velocity dispersion, σ , that is,

$$\log r_e = a \log \sigma + b \langle\mu_e\rangle + c, \quad (16)$$

where a and b are the FP slopes and c is the intercept.

In Table 1, we present the FP data for the Norma ETGs ($N=31$). Presented in this table are the central velocity dispersions and the photometric results obtained using the IRSF NIR J and K_s -band images. The Galactic extinction correction applied to $\langle\mu_e\rangle$ is from the re-calibration presented in Section 3.4, i.e., $A_J = 0.937 f E(B-V)$ and $A_{K_s} = 0.382 f E(B-V)$ where $f = 0.81 \pm 0.06$ for the Norma cluster sample and $f = 0.93 \pm 0.05$ for the Coma cluster calibration sample.

4.2. Fundamental Plane – Fit results

The FP was fitted using the inverse least-squares fit. The top and bottom panels of Figure 4 show the FP projection for the J - and K_s -band, respectively. The black open circles represent the Coma cluster galaxies while the red filled circles are the Norma cluster galaxies shifted to the Coma distance. This was done assuming the Coma cluster has a zero peculiar velocity.

The combined K_s -band FP analysis was performed using the combined IRSF and NTT data. In combining the two data sets, the latter were given preference due to the higher resolution imaging. The FP projection obtained from the combined K_s -band analysis is shown in Figure 5. The black open circles represent the Coma cluster galaxies while the red filled circles represent the Norma cluster galaxies after shifting them to the Coma cluster’s distance. A summary of results for the IRSF J and K_s -band as well as the combined K_s -band FP fit parameters is presented in Table 2. The derived values for the FP parameters a , and b are comparable with other previous FP studies in the near-infrared (see e.g., La Barbera et al. 2010; Magoulas et al. 2012).

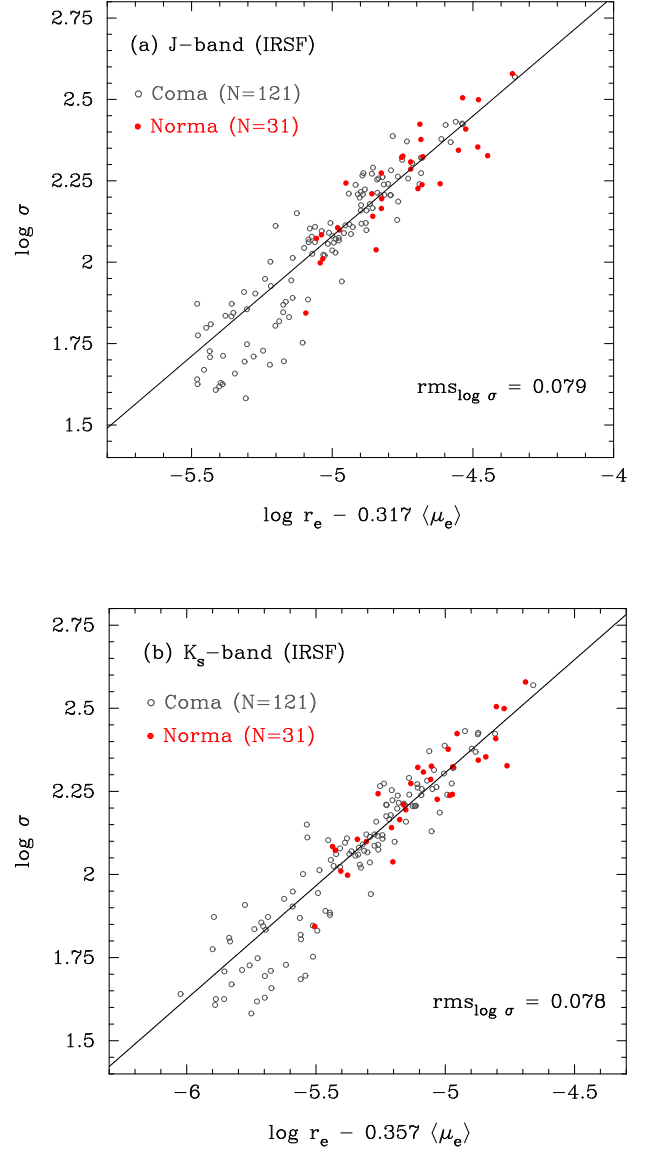


Figure 4. The J and K_s -band FP based on 31 ETGs from the IRSF data (for the Norma cluster) and 121 ETGs from 2MASS (for the Coma calibration sample). The top (a) and bottom (b) panels represent the J - and K_s -band FP projections, respectively. The red filled circles represent the Norma cluster ETGs after shifting them to the Coma cluster’s distance. The black open circles represent the Coma cluster galaxies.

5. NORMA CLUSTER: DISTANCE AND PECULIAR VELOCITY

Table 2 shows the different zero-point offsets measured using the J and K_s -band FP analysis. These are in excellent agreement with each other. The best measured value (least scatter/error) is from the combined K_s -band FP analysis using 41 ETGs within the Norma cluster. We adopted this value to measure the distance and peculiar velocity for the Norma

Table 1. Norma cluster J and K_s -band photometry results from fitting and extrapolating the galaxy surface brightness profiles. NIR images taken using the IRSF telescope were used for the photometry analysis. The total extrapolated magnitudes presented here have been corrected for only, the star-subtraction and sky background effects. The J and K_s -band mean effective surface brightness in mag arcsec^{-2} have been corrected for the Galactic extinction, redshift, and the cosmological dimming effects. The Galactic extinction values are from the re-calibration presented under Section 3.4, where, $A_J = 0.937 f E(B - V)$ and $A_{K_s} = 0.382 f E(B - V)$. Both the aperture correction and run offset have been applied to the central velocity dispersion values (in dex) presented here. The FP variables, that is, effective radii, mean effective surface brightnesses and the central velocity dispersions presented here have been fully corrected. These were used in the final FP fitting and analysis.

Identification	Total magnitude		Effective radius		Mean eff. surf. brightness		Extinction		$\log \sigma$
	J	K_s	J	K_s	J	K_s	A_J	A_{K_s}	
(1)	(2)	(3)	(4)	(5)	(6)	(7)	(8)	(9)	(10)
WKK6019	10.87±0.06	9.82±0.03	4.56±0.50	4.22±0.23	15.98±0.24	14.81±0.12	0.172	0.070	2.409±0.010
WKK6047	12.81±0.06	11.83±0.03	3.07±0.22	2.92±0.13	17.09±0.16	16.04±0.10	0.173	0.070	2.010±0.015
WKK6075	12.95±0.06	11.92±0.03	2.32±0.27	2.14±0.06	16.56±0.26	15.38±0.07	0.181	0.074	2.099±0.017
WKK6116	10.50±0.06	9.47±0.04	7.48±1.00	7.59±0.70	16.71±0.30	15.71±0.21	0.163	0.066	2.344±0.012
WKK6148	12.67±0.05	11.69±0.03	3.84±0.18	3.33±0.14	17.39±0.11	16.13±0.10	0.155	0.063	1.998±0.019
WKK6180	11.16±0.06	10.13±0.03	6.84±0.69	7.18±0.37	17.12±0.23	16.24±0.12	0.159	0.065	2.308±0.011
WKK6183	11.13±0.06	10.16±0.03	5.32±0.82	5.58±0.42	16.68±0.34	15.66±0.17	0.155	0.063	2.377±0.012
WKK6193	11.10±0.07	10.00±0.03	6.48±0.68	6.60±0.28	16.97±0.24	15.99±0.10	0.159	0.065	2.226±0.010
WKK6204	10.35±0.07	9.63±0.28	6.87±1.12	5.22±3.16	16.37±0.36	14.98±1.34	0.160	0.065	2.499±0.009
WKK6207	11.05±0.07	9.90±0.03	4.38±0.83	6.39±0.52	16.21±0.42	15.78±0.18	0.152	0.062	2.241±0.012
WKK6221	11.31±0.06	10.77±0.04	9.14±1.05	7.47±0.38	17.89±0.26	16.62±0.11	0.164	0.067	2.038±0.017
WKK6229	12.56±0.07	11.59±0.03	2.30±0.25	1.97±0.09	16.19±0.24	14.88±0.11	0.156	0.063	2.210±0.015
WKK6233	12.73±0.07	11.91±0.04	2.69±0.22	2.14±0.07	16.66±0.19	15.26±0.08	0.152	0.062	2.243±0.014
WKK6235	11.91±0.06	10.96±0.03	4.73±0.42	4.39±0.21	17.07±0.20	15.99±0.11	0.170	0.069	2.141±0.018
WKK6242	11.82±0.07	10.90±0.03	2.74±0.24	2.16±0.15	15.86±0.20	14.41±0.15	0.151	0.061	2.424±0.011
WKK6250	11.56±0.05	10.55±0.02	3.58±0.31	3.41±0.13	16.15±0.20	15.01±0.08	0.159	0.065	2.324±0.010
WKK6252	13.00±0.06	12.18±0.03	2.80±0.24	2.44±0.16	17.04±0.19	15.88±0.14	0.153	0.063	2.073±0.012
WKK6269	8.97±0.06	8.14±0.03	20.40±2.47	17.57±1.03	17.44±0.27	16.22±0.13	0.148	0.060	2.579±0.011
WKK6275	11.40±0.06	10.22±0.03	7.74±0.78	8.39±0.60	17.62±0.23	16.68±0.16	0.149	0.061	2.165±0.014
WKK6282	12.17±0.06	11.22±0.03	3.05±0.33	2.60±0.17	16.42±0.24	15.14±0.15	0.147	0.060	2.274±0.012
WKK6297	12.69±0.05	11.78±0.02	4.38±0.25	4.01±0.18	17.72±0.14	16.71±0.10	0.149	0.061	1.844±0.026
WKK6305	10.23±0.05	9.24±0.11	6.77±0.79	7.93±1.49	16.25±0.26	15.45±0.42	0.198	0.081	2.327±0.009
WKK6318	9.61±0.06	8.73±0.03	15.84±1.76	13.75±0.79	17.49±0.25	16.35±0.13	0.180	0.073	2.354±0.013
WKK6342	12.08±0.05	11.06±0.02	2.59±0.13	3.05±0.15	15.98±0.12	15.11±0.11	0.152	0.062	2.326±0.009
WKK6360	10.92±0.06	10.02±0.02	4.19±0.66	3.60±0.15	15.91±0.35	14.61±0.10	0.154	0.063	2.505±0.009
WKK6383	11.94±0.06	10.78±0.03	4.04±0.26	4.59±0.22	16.77±0.15	15.88±0.11	0.176	0.072	2.195±0.012
WKK6402	11.56±0.05	10.62±0.02	3.70±0.29	3.23±0.15	16.20±0.18	14.98±0.10	0.190	0.077	2.238±0.011
WKK6429	12.30±0.04	11.63±0.04	5.04±0.37	5.56±0.17	17.73±0.16	16.91±0.09	0.159	0.065	2.084±0.012
WKK6431	11.74±0.05	10.78±0.03	3.56±0.24	3.18±0.19	16.28±0.16	15.17±0.13	0.184	0.075	2.286±0.010
WKK6459	11.37±0.06	10.45±0.04	6.18±0.85	6.25±0.21	17.09±0.31	16.13±0.08	0.200	0.081	2.322±0.010
WKK6477	12.67±0.05	11.73±0.04	3.02±0.32	2.68±0.13	16.90±0.23	15.76±0.11	0.179	0.073	2.106±0.019

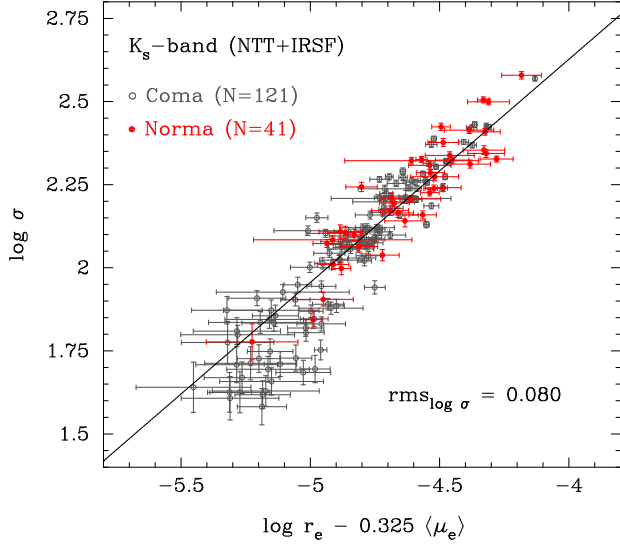


Figure 5. Same as Figure 4 but for the combined K_s -band FP projection.

Table 2. The J - and K_s -band FP fit parameters (a and b) as well as the zero-point offset. The first column indicates the source of the data used while column 5 is the FP zero-point offset. Columns 6 and 7 are the scatter and the corresponding percentage uncertainty in the distance to the individual Norma cluster galaxies, respectively. Column 8 indicates the number of Norma cluster galaxies used in our analysis; this is 121 for the Coma cluster.

Sample	Filter	a	b	Δc	rms	% err	N
(1)	(2)	(3)	(4)	(5)	(6)	(7)	(8)
NTT	K_s	1.465 ± 0.059	0.326 ± 0.020	0.154 ± 0.014	0.083	28	31*
IRSF	J	1.356 ± 0.058	0.317 ± 0.018	0.149 ± 0.016	0.079	25	31
IRSF	K_s	1.470 ± 0.053	0.357 ± 0.019	0.145 ± 0.014	0.078	26	31
NTT+IRSF	K_s	1.490 ± 0.053	0.325 ± 0.017	0.163 ± 0.013	0.080	27	41

* — All data in this row were taken from Mutabazi et al. (2014).

cluster. This implies that

$$\log D_A(\text{Coma}) - \log D_A(\text{Norma}) = 0.163 \pm 0.013, \quad (17)$$

where $D_A(\text{Coma})$ and $D_A(\text{Norma})$ are the angular diameter distances for the Coma and Norma clusters, respectively. The angular diameter distances were measured following Wright (2006). The distance (Hubble redshift, z_H) and the peculiar velocity for the Norma cluster were derived using the same method described in Mutabazi et al. (2014). That is, the peculiar velocity for the Norma cluster was computed using

$$v_{\text{pec}} = c z_{\text{pec}}, \quad (18)$$

where c is the speed of light and

$$z_{\text{pec}} = \frac{1 + z_{\text{CMB}}}{1 + z_H} - 1. \quad (19)$$

The resulting Norma cluster's peculiar velocity after applying the homogeneous Malmquist bias correction (see

Table 3. The J - and K_s -band FP offsets (column 3) and the corresponding measured peculiar velocity (column 5). The homogeneous Malmquist bias correction shown in column 6 has not been applied (this should be subtracted from the peculiar velocity presented in column 5).

Sample	Filter	Δc [dex]	z_H	v_{pec} [km s^{-1}]	Malm. bias [km s^{-1}]	N
(1)	(2)	(3)	(4)	(5)	(6)	(7)
NTT	K_s	0.154 ± 0.014	0.01667 ± 0.00055	-43 ± 170	29	31*
IRSF	J	0.149 ± 0.016	0.01684 ± 0.00062	-95 ± 187	33	31
IRSF	K_s	0.145 ± 0.014	0.01704 ± 0.00058	-152 ± 173	30	31
NTT+IRSF	K_s	0.163 ± 0.013	0.01632 ± 0.00050	$+58 \pm 151$	14	41

* — All data in this row were taken from Mutabazi et al. (2014).

Hudson et al. 1997, for details) presented in Table 3 is $44 \pm 151 \text{ km s}^{-1}$ (distance of $4915 \pm 121 \text{ km s}^{-1}$ or $d = 69.7 \pm 1.7 \text{ Mpc}$).

6. DISCUSSION AND CONCLUSIONS

We have measured a small peculiar velocity of the Norma cluster of $+44 \pm 151 \text{ km s}^{-1}$ which within errors, is consistent with zero and in excellent agreement with our previous measurement of $-72 \pm 170 \text{ km s}^{-1}$ (Mutabazi et al. 2014). Our analysis and results have demonstrated, that, despite the challenges of the large Galactic extinction and severe stellar contamination, distances using the FP and TF relations can be derived reliably for galaxies that lie relatively close to the Galactic plane. We have carefully considered the possible sources of measurement and systematic errors. Results from simulations of ETGs showed that the effect of star-subtraction is very small, ranging from $-0^{\text{m}}011$ (NTT K_s -band data) to $-0^{\text{m}}014$ (IRSF K_s -band data), which offsets the measured peculiar velocity by $\sim 41 \text{ km s}^{-1}$ to $\sim 52 \text{ km s}^{-1}$, respectively. The systematic effect arising from possible gradients in the sky background is very small, i.e., $\sim -0^{\text{m}}008$, which corresponds to a change in Norma's measured peculiar velocity of $\sim 30 \text{ km s}^{-1}$.

Using the NIR J and K_s -band images obtained using the IRSF telescope has also helped re-calibrate the Schlegel et al. (1998) extinction values as described in Section 3.4. For the Norma cluster sample, the measured extinction correction factor is 0.81 for the Schlegel et al. maps, which is in good agreement with the Schlafly & Finkbeiner (2011) extinction values. The combined K_s -band FP sample resulted in the largest cluster sample ($N = 41$) used in the peculiar velocity studies at relatively low Galactic latitudes to date, and hence the most precise distance and peculiar velocity of the Norma cluster measured to date.

Figure 6 shows the peculiar velocities for Clusters/Groups in the GA region. The peculiar velocity measurements were taken from the literature. Shown are the velocity measurements from ENEARc (Bernardi et al. 2002), SMAC (Hudson et al. 2004), SFI++ (Springob et al. 2007), and our Norma cluster measurement (red filled circle). The dashed

horizontal lines represent $\pm 3\sigma$ where $\sigma = 151 \text{ km s}^{-1}$ is the error on the Norma cluster’s peculiar velocity derived using the combined K_s -band FP analysis. N_ϕ is the angular separation between the cluster and Norma. The improved sample of 41 ETGs taken from within $\frac{2}{3}$ of the Norma cluster’s Abell radius makes this the most precise measurement for the distance and peculiar velocity of the Norma cluster to date.

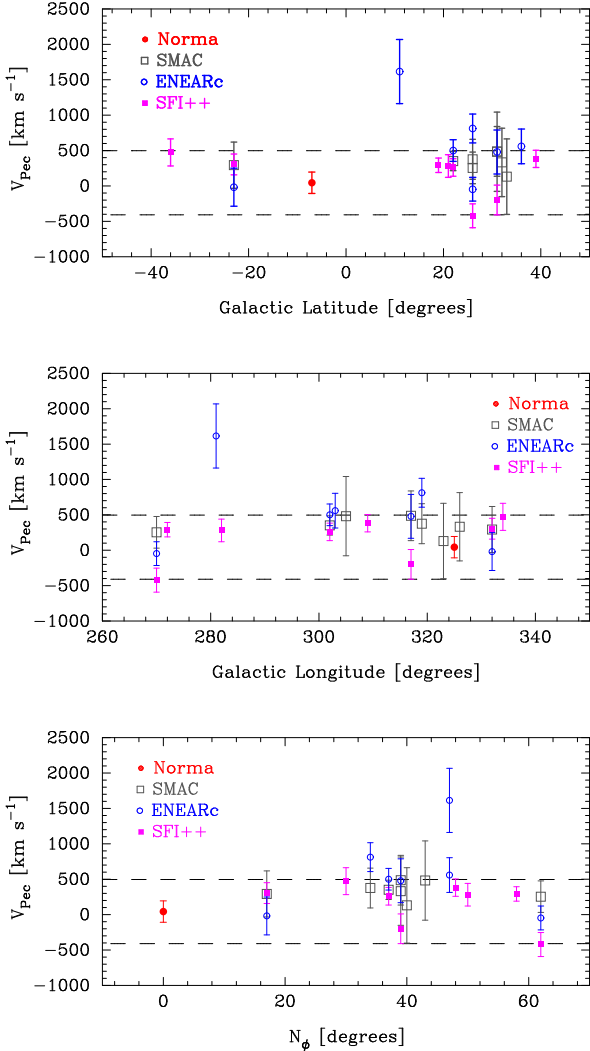


Figure 6. Peculiar velocities for Clusters/Groups in the GA region. The Norma cluster is represented by the red filled circle. The dashed horizontal lines represent $\pm 3\sigma$ where σ is the error on the Norma cluster’s peculiar velocity measured using the combined K_s -band FP analysis. N_ϕ is the angle on the sky between the cluster and Norma.

In the study by Carrick et al. (2015) the residual bulk flow due to structures not covered by the 2M++ redshift sample has a velocity of $159 \pm 23 \text{ km s}^{-1}$ in the direction $\ell = 303^\circ \pm 11^\circ$, $b = 6^\circ \pm 11^\circ$. This is $\sim 25^\circ$ from Norma, and therefore corresponds to $\sim 144 \pm 21 \text{ km s}^{-1}$. This is the external bulk flow contribution on the Norma peculiar ve-

locity arising from structures beyond the volume covered by the 2M++ redshift catalogue (Lavaux & Hudson 2011). Similar residual bulk flows have been reported with a bulk flow contribution on the Norma cluster of e.g., $136 \pm 39 \text{ km s}^{-1}$ (Turnbull et al. 2012), $154 \pm 10 \text{ km s}^{-1}$ (Boruah et al. 2019), $147 \pm 12 \text{ km s}^{-1}$ (Said et al. 2020), and $161 \pm 11 \text{ km s}^{-1}$ (Said et al. 2020). These are all significantly different from zero and are, within the error margin (1σ), consistent with our Norma’s peculiar velocity of $44 \pm 151 \text{ km s}^{-1}$. Dedicated surveys such as Taipan (da Cunha et al. 2017; Taylor 2020) and WALLABY (Duffy et al. 2012; Koribalski et al. 2020) will help improve the accuracy of distance measurements and hence enable us infer more accurate peculiar velocities.

ACKNOWLEDGMENTS

TM acknowledges financial support from the Square Kilometre Array South Africa (SKA SA). Travel costs to Sutherland site of the South African Astronomical Observatory were funded by the multi-wavelength funding (Department of Astronomy, University of Cape Town). Funding for SDSS-III has been provided by the Alfred P. Sloan Foundation, the Participating Institutions, the National Science Foundation, and the U.S. Department of Energy Office of Science. The SDSS-III web site is <http://www.sdss3.org/>. SDSS-III is managed by the Astrophysical Research Consortium for the Participating Institutions of the SDSS-III Collaboration including the University of Arizona, the Brazilian Participation Group, Brookhaven National Laboratory, Carnegie Mellon University, University of Florida, the French Participation Group, the German Participation Group, Harvard University, the Instituto de Astrofísica de Canarias, the Michigan State/Notre Dame/JINA Participation Group, Johns Hopkins University, Lawrence Berkeley National Laboratory, Max Planck Institute for Astrophysics, Max Planck Institute for Extraterrestrial Physics, New Mexico State University, New York University, Ohio State University, Pennsylvania State University, University of Portsmouth, Princeton University, the Spanish Participation Group, University of Tokyo, University of Utah, Vanderbilt University, University of Virginia, University of Washington, and Yale University. This publication has made use of the NASA/IPAC ExtraGalactic Data base (NED), and also data products from the 2MASS, a joint project of the University of Massachusetts and the Infrared Processing and Analysis Center California Institute of Technology, funded by the National Aeronautics and Space Administration and the National Science Foundation.

Software: GALFIT (Peng et al. 2010), MATPLOTLIB (Hunter 2007), SCIPY (Virtanen et al. 2017), NUMPY (Oliphant 2006; van der Walt et al. 2011), PGPLOT

(Pearson 2011), ELLIPSE task under IRAF's STSDAS package (Jedrzejewski 1987).

Facilities: 1.4m Infrared Survey Facility (IRSF) at South Africa Astronomical Observatory Sutherland site, European Southern Observatory (ESO) 3.6m New Technology Telescope (NTT) at La Silla Observatory, Australian National University (ANU) 3.9m Anglo-Australian Telescope (AAT) at Siding Spring Observatory (SSO).

REFERENCES

- Abell, G. O., Corwin, Jr., H. G., & Olowin, R. P. 1989, *ApJS*, 70, 1, doi: [10.1086/191333](https://doi.org/10.1086/191333)
- Aihara, H., Allende Prieto, C., An, D., et al. 2011, *ApJS*, 193, 29, doi: [10.1088/0067-0049/193/2/29](https://doi.org/10.1088/0067-0049/193/2/29)
- Bardelli, S., Zucca, E., Zamorani, G., Moscardini, L., & Scaramella, R. 2000, *MNRAS*, 312, 540, doi: [10.1046/j.1365-8711.2000.03174.x](https://doi.org/10.1046/j.1365-8711.2000.03174.x)
- Bernardi, M., Alonso, M. V., da Costa, L. N., et al. 2002, *AJ*, 123, 2159, doi: [10.1086/339697](https://doi.org/10.1086/339697)
- Boehringer, H., Neumann, D. M., Schindler, S., & Kraan-Korteweg, R. C. 1996, *ApJ*, 467, 168, doi: [10.1086/177592](https://doi.org/10.1086/177592)
- Bolejko, K., & Hellaby, C. 2008, *General Relativity and Gravitation*, 40, 1771, doi: [10.1007/s10714-007-0573-5](https://doi.org/10.1007/s10714-007-0573-5)
- Bonifacio, P., Monai, S., & Beers, T. C. 2000, *AJ*, 120, 2065, doi: [10.1086/301566](https://doi.org/10.1086/301566)
- Boruah, S. S., Hudson, M. J., & Lavaux, G. 2019, arXiv e-prints, arXiv:1912.09383. <https://arxiv.org/abs/1912.09383>
- Carpenter, J. M. 2001, *AJ*, 121, 2851, doi: [10.1086/320383](https://doi.org/10.1086/320383)
- Carrick, J., Turnbull, S. J., Lavaux, G., & Hudson, M. J. 2015, *MNRAS*, 450, 317, doi: [10.1093/mnras/stv547](https://doi.org/10.1093/mnras/stv547)
- Chilingarian, I. V., Melchior, A.-L., & Zolotukhin, I. Y. 2010, *MNRAS*, 405, 1409, doi: [10.1111/j.1365-2966.2010.16506.x](https://doi.org/10.1111/j.1365-2966.2010.16506.x)
- Courtois, H. M., Kraan-Korteweg, R. C., Dupuy, A., Graziani, R., & Libeskind, N. I. 2019, *MNRAS*, 490, L57, doi: [10.1093/mnras/slz146](https://doi.org/10.1093/mnras/slz146)
- Courtois, H. M., Tully, R. B., Hoffman, Y., et al. 2017, *ApJ*, 847, L6, doi: [10.3847/2041-8213/aa88b2](https://doi.org/10.3847/2041-8213/aa88b2)
- da Cunha, E., Hopkins, A. M., Colless, M., et al. 2017, *PASA*, 34, e047, doi: [10.1017/pasa.2017.41](https://doi.org/10.1017/pasa.2017.41)
- Djorgovski, S., & Davis, M. 1987, *ApJ*, 313, 59, doi: [10.1086/164948](https://doi.org/10.1086/164948)
- Dressler, A. 1980, *ApJS*, 42, 565, doi: [10.1086/190663](https://doi.org/10.1086/190663)
- Dressler, A., Lynden-Bell, D., Burstein, D., et al. 1987, *ApJ*, 313, 42, doi: [10.1086/164947](https://doi.org/10.1086/164947)
- Duffy, A. R., Meyer, M. J., Staveley-Smith, L., et al. 2012, *MNRAS*, 426, 3385, doi: [10.1111/j.1365-2966.2012.21987.x](https://doi.org/10.1111/j.1365-2966.2012.21987.x)
- Erdoğdu, P., Lahav, O., Huchra, J. P., et al. 2006, *MNRAS*, 373, 45, doi: [10.1111/j.1365-2966.2006.11049.x](https://doi.org/10.1111/j.1365-2966.2006.11049.x)
- Fitzpatrick, E. L. 1999, *PASP*, 111, 63, doi: [10.1086/316293](https://doi.org/10.1086/316293)
- Glass, I. S. 1999, *Handbook of Infrared Astronomy*, ed. Glass, I. S. Hinshaw, G., Weiland, J. L., Hill, R. S., et al. 2009, *ApJS*, 180, 225, doi: [10.1088/0067-0049/180/2/225](https://doi.org/10.1088/0067-0049/180/2/225)
- Hoffman, Y., Pomarède, D., Tully, R. B., & Courtois, H. M. 2017, *Nature Astronomy*, 1, 0036, doi: [10.1038/s41550-016-0036](https://doi.org/10.1038/s41550-016-0036)
- Hudson, M. J., Lucey, J. R., Smith, R. J., & Steel, J. 1997, *MNRAS*, 291, 488
- Hudson, M. J., Smith, R. J., Lucey, J. R., & Branchini, E. 2004, *MNRAS*, 352, 61, doi: [10.1111/j.1365-2966.2004.07893.x](https://doi.org/10.1111/j.1365-2966.2004.07893.x)
- Hunter, J. D. 2007, *Computing in Science and Engineering*, 9, 90, doi: [10.1109/MCSE.2007.55](https://doi.org/10.1109/MCSE.2007.55)
- Jedrzejewski, R. I. 1987, *MNRAS*, 226, 747, doi: [10.1093/mnras/226.4.747](https://doi.org/10.1093/mnras/226.4.747)
- Kocevski, D. D., & Ebeling, H. 2006, *ApJ*, 645, 1043, doi: [10.1086/503666](https://doi.org/10.1086/503666)
- Kogut, A., Lineweaver, C., Smoot, G. F., et al. 1993, *ApJ*, 419, 1, doi: [10.1086/173453](https://doi.org/10.1086/173453)
- Kolatt, T., Dekel, A., & Lahav, O. 1995, *MNRAS*, 275, 797
- Koribalski, B. S., Staveley-Smith, L., Westmeier, T., et al. 2020, *Ap&SS*, 365, 118, doi: [10.1007/s10509-020-03831-4](https://doi.org/10.1007/s10509-020-03831-4)
- Kraan-Korteweg, R. C., Cluver, M. E., Bilicki, M., et al. 2017, *MNRAS*, 466, L29, doi: [10.1093/mnras/rlw229](https://doi.org/10.1093/mnras/rlw229)
- Kraan-Korteweg, R. C., van Driel, W., Schröder, A. C., Ramatsoku, M., & Henning, P. A. 2018, *MNRAS*, 481, 1262, doi: [10.1093/mnras/sty2285](https://doi.org/10.1093/mnras/sty2285)
- Kraan-Korteweg, R. C., Woudt, P. A., Cayatte, V., et al. 1996, *Nature*, 379, 519, doi: [10.1038/379519a0](https://doi.org/10.1038/379519a0)
- La Barbera, F., de Carvalho, R. R., de La Rosa, I. G., & Lopes, P. A. A. 2010, *MNRAS*, 408, 1335, doi: [10.1111/j.1365-2966.2010.17091.x](https://doi.org/10.1111/j.1365-2966.2010.17091.x)
- Lavaux, G., & Hudson, M. J. 2011, *MNRAS*, 416, 2840, doi: [10.1111/j.1365-2966.2011.19233.x](https://doi.org/10.1111/j.1365-2966.2011.19233.x)
- Lavaux, G., Tully, R. B., Mohayaee, R., & Colombi, S. 2010, *ApJ*, 709, 483, doi: [10.1088/0004-637X/709/1/483](https://doi.org/10.1088/0004-637X/709/1/483)
- Lewis, I. J., Cannon, R. D., Taylor, K., et al. 2002, *MNRAS*, 333, 279, doi: [10.1046/j.1365-8711.2002.05333.x](https://doi.org/10.1046/j.1365-8711.2002.05333.x)
- Lucey, J., Radburn-Smith, D., & Hudson, M. 2005, in *Astronomical Society of the Pacific Conference Series*, Vol. 329, *Nearby Large-Scale Structures and the Zone of Avoidance*, ed. A. P. Fairall & P. A. Woudt, 21
- Macri, L. M., Kraan-Korteweg, R. C., Lambert, T., et al. 2019, *ApJS*, 245, 6, doi: [10.3847/1538-4365/ab465a](https://doi.org/10.3847/1538-4365/ab465a)

- Magoulas, C., Springob, C. M., Colless, M., et al. 2012, *MNRAS*, 427, 245, doi: [10.1111/j.1365-2966.2012.21421.x](https://doi.org/10.1111/j.1365-2966.2012.21421.x)
- Mutabazi, T., Blyth, S. L., Woudt, P. A., et al. 2014, *MNRAS*, 439, 3666, doi: [10.1093/mnras/stu217](https://doi.org/10.1093/mnras/stu217)
- Nagashima, C., Nagayama, T., Nakajima, Y., et al. 1999, in *Star Formation 1999*, ed. T. Nakamoto, 397–398
- Oliphant, T. 2006, *Guide to NumPy* (Massachusetts Institute of Technology, Dec 7, 2006)
- Pearson, T. 2011, *PGPLOT: Device-independent Graphics Package for Simple Scientific Graphs*. <http://ascl.net/1103.002>
- Peng, C. Y., Ho, L. C., Impey, C. D., & Rix, H. 2010, *AJ*, 139, 2097, doi: [10.1088/0004-6256/139/6/2097](https://doi.org/10.1088/0004-6256/139/6/2097)
- Qin, F., Howlett, C., Staveley-Smith, L., & Hong, T. 2018, *MNRAS*, 477, 5150, doi: [10.1093/mnras/sty928](https://doi.org/10.1093/mnras/sty928)
- Raychaudhury, S. 1989, *Nature*, 342, 251, doi: [10.1038/342251a0](https://doi.org/10.1038/342251a0)
- Said, K., Colless, M., Magoulas, C., Lucey, J. R., & Hudson, M. J. 2020, *MNRAS*, 497, 1275, doi: [10.1093/mnras/staa2032](https://doi.org/10.1093/mnras/staa2032)
- Said, K., Kraan-Korteweg, R. C., Jarrett, T. H., Staveley-Smith, L., & Williams, W. L. 2016a, *MNRAS*, 462, 3386, doi: [10.1093/mnras/stw1887](https://doi.org/10.1093/mnras/stw1887)
- Said, K., Kraan-Korteweg, R. C., Staveley-Smith, L., et al. 2016b, *MNRAS*, 457, 2366, doi: [10.1093/mnras/stw105](https://doi.org/10.1093/mnras/stw105)
- Scaramella, R., Baiesi-Pillastrini, G., Chincarini, G., Vettolani, G., & Zamorani, G. 1989, *Nature*, 338, 562, doi: [10.1038/338562a0](https://doi.org/10.1038/338562a0)
- Schlafly, E. F., & Finkbeiner, D. P. 2011, *ApJ*, 737, 103, doi: [10.1088/0004-637X/737/2/103](https://doi.org/10.1088/0004-637X/737/2/103)
- Schlegel, D. J., Finkbeiner, D. P., & Davis, M. 1998, *ApJ*, 500, 525, doi: [10.1086/305772](https://doi.org/10.1086/305772)
- Schröder, A. C., Mamon, G. A., Kraan-Korteweg, R. C., & Woudt, P. A. 2007, *A&A*, 466, 481, doi: [10.1051/0004-6361:20065980](https://doi.org/10.1051/0004-6361:20065980)
- Schröder, A. C., van Driel, W., & Kraan-Korteweg, R. C. 2019, *MNRAS*, 482, 5167, doi: [10.1093/mnras/sty3022](https://doi.org/10.1093/mnras/sty3022)
- Shapley, H. 1930, *Harvard College Observatory Bulletin*, 874, 9
- Skrutskie, M. F., Cutri, R. M., Stiening, R., et al. 2006, *AJ*, 131, 1163, doi: [10.1086/498708](https://doi.org/10.1086/498708)
- Smith, R. J., Hudson, M. J., Lucey, J. R., Schlegel, D. J., & Davies, R. L. 2000, in *Astronomical Society of the Pacific Conference Series*, Vol. 201, *Cosmic Flows Workshop*, ed. S. Courteau & J. Willick, 39
- Sorce, J. G., Colless, M., Kraan-Korteweg, R. C., & Gottlöber, S. 2017, *MNRAS*, 471, 3087, doi: [10.1093/mnras/stx1800](https://doi.org/10.1093/mnras/stx1800)
- Springob, C. M., Masters, K. L., Haynes, M. P., Giovanelli, R., & Marinoni, C. 2007, *ApJS*, 172, 599, doi: [10.1086/519527](https://doi.org/10.1086/519527)
- Springob, C. M., Magoulas, C., Colless, M., et al. 2014, *MNRAS*, 445, 2677, doi: [10.1093/mnras/stu1743](https://doi.org/10.1093/mnras/stu1743)
- Springob, C. M., Hong, T., Staveley-Smith, L., et al. 2016, *MNRAS*, 456, 1886, doi: [10.1093/mnras/stv2648](https://doi.org/10.1093/mnras/stv2648)
- Staveley-Smith, L., Kraan-Korteweg, R. C., Schröder, A. C., et al. 2016, *AJ*, 151, 52, doi: [10.3847/0004-6256/151/3/52](https://doi.org/10.3847/0004-6256/151/3/52)
- Tamura, T., Fukazawa, Y., Kaneda, H., et al. 1998, *PASJ*, 50, 195, doi: [10.1093/pasj/50.2.195](https://doi.org/10.1093/pasj/50.2.195)
- Taylor, E. 2020, in *The Build-Up of Galaxies through Multiple Tracers and Facilities*, 75, doi: [10.5281/zenodo.3756572](https://doi.org/10.5281/zenodo.3756572)
- Tully, R. B., Courtois, H. M., & Sorce, J. G. 2016, *AJ*, 152, 50, doi: [10.3847/0004-6256/152/2/50](https://doi.org/10.3847/0004-6256/152/2/50)
- Tully, R. B., Pomarède, D., Graziani, R., et al. 2019, *ApJ*, 880, 24, doi: [10.3847/1538-4357/ab2597](https://doi.org/10.3847/1538-4357/ab2597)
- Turnbull, S. J., Hudson, M. J., Feldman, H. A., et al. 2012, *MNRAS*, 420, 447, doi: [10.1111/j.1365-2966.2011.20050.x](https://doi.org/10.1111/j.1365-2966.2011.20050.x)
- van der Walt, S., Colbert, S. C., & Varoquaux, G. 2011, *Computing in Science and Engineering*, 13, 22, doi: [10.1109/MCSE.2011.37](https://doi.org/10.1109/MCSE.2011.37)
- Virtanen, P., Gommers, R., Oliphant, T. E., et al. 2017, *Scipy/Scipy: Scipy 0.19.0, v0.19.0*, Zenodo, doi: [10.5281/zenodo.376244](https://doi.org/10.5281/zenodo.376244)
- Woudt, P. A., Kraan-Korteweg, R. C., Lucey, J., Fairall, A. P., & Moore, S. A. W. 2008, *MNRAS*, 383, 445, doi: [10.1111/j.1365-2966.2007.12571.x](https://doi.org/10.1111/j.1365-2966.2007.12571.x)
- Wright, E. L. 2006, *PASP*, 118, 1711, doi: [10.1086/510102](https://doi.org/10.1086/510102)
- Yasuda, N., Fukugita, M., & Schneider, D. P. 2007, *AJ*, 134, 698, doi: [10.1086/519836](https://doi.org/10.1086/519836)

APPENDIX

A. COMA CLUSTER ETGS – CALIBRATION SAMPLE

The Coma cluster galaxies used in our calibration sample are those which (1) are classified as E/S0 or S0 in [Dressler \(1980\)](#) (2) are Coma cluster members based on their redshifts, (3) have central velocity dispersions available in SDSS DR8 ([Aihara et al. 2011](#)), and (4) we were able to successfully measure their total extrapolated magnitudes and effective radii using the 2MASS Extended Source ([Skrutskie et al. 2006](#)) Atlas images. The photometry measurements (total extrapolated magnitudes, effective radii, and the computed mean effective surface brightness) in the J and K_s -bands) obtained from surface brightness profile fitting of the Coma cluster ETGs are summarised in Table 4.

Table 4. Coma cluster J and K_s photometry results from fitting and extrapolating the galaxy surface brightness profiles using the 2MASS Atlas images. No corrections have been applied to the total magnitudes presented here.

Identification	Total magnitude		Effective radius		Mean eff. surf. brightness		$\log \sigma$
	J	K_s	J	K_s	J	K_s	
(1)	(2)	(3)	(4)	(5)	(6)	(7)	(8)
2MASXJ13023273+2717443	14.15±0.08	13.48±0.15	3.98±0.21	3.23±0.59	19.05±0.14	17.83±0.42	1.709±0.055
2MASXJ13020552+2717499	13.93±0.06	13.51±0.14	4.19±0.08	2.21±0.52	18.95±0.07	17.04±0.53	1.836±0.033
2MASXJ13000623+2718022	13.63±0.04	12.82±0.07	4.59±0.18	4.46±0.46	18.83±0.09	17.86±0.23	1.748±0.038
2MASXJ12593730+2720097	14.74±0.11	14.27±0.24	2.25±0.17	2.29±0.58	18.41±0.20	17.89±0.60	1.640±0.076
2MASXJ13010615+2723522	14.31±0.09	13.83±0.17	3.26±0.44	2.15±0.41	18.76±0.31	17.28±0.45	1.809±0.041
2MASXJ12564777+2725158	14.25±0.10	13.48±0.12	3.11±0.33	2.24±0.27	18.61±0.25	17.03±0.29	1.618±0.042
2MASXJ12583209+2727227	13.38±0.05	12.57±0.05	2.00±0.10	1.87±0.20	16.78±0.11	15.74±0.23	2.056±0.014
2MASXJ12573614+2729058	13.15±0.03	12.15±0.04	1.97±0.04	2.05±0.04	16.53±0.05	15.52±0.06	2.210±0.009
2MASXJ12570940+2727587	12.24±0.02	11.16±0.02	2.55±0.32	3.02±0.02	16.17±0.27	15.37±0.02	2.304±0.008
2MASXJ13002689+2730556	13.49±0.05	12.52±0.05	1.86±0.09	2.40±0.21	16.74±0.11	16.21±0.20	2.023±0.014
2MASXJ12580974+2732585	14.25±0.08	13.28±0.10	3.48±0.30	2.95±0.27	18.87±0.20	17.45±0.22	1.727±0.042
2MASXJ12573584+2729358	11.97±0.02	10.90±0.02	3.07±0.05	3.57±0.02	16.31±0.04	15.47±0.02	2.321±0.009
2MASXJ12572435+2729517	9.85±0.00	9.07±0.00	27.31±0.05	21.19±0.20	18.93±0.00	17.51±0.02	2.431±0.008
2MASXJ12570431+2731328	14.24±0.08	13.63±0.15	4.32±0.48	3.17±0.49	19.31±0.25	17.92±0.37	1.872±0.041
2MASXJ12563418+2732200	12.71±0.03	11.61±0.03	2.80±0.08	3.59±0.07	16.85±0.07	16.20±0.05	2.208±0.009
2MASXJ13014841+2736147	13.51±0.04	12.82±0.07	3.21±0.16	2.41±0.14	17.94±0.12	16.51±0.15	1.846±0.022
2MASXJ13011224+2736162	13.76±0.06	12.53±0.05	3.09±0.15	4.37±0.31	18.11±0.12	17.53±0.16	1.729±0.039
2MASXJ13001914+2733135	12.88±0.03	11.79±0.03	3.28±0.08	3.90±0.24	17.37±0.06	16.59±0.14	2.030±0.013
2MASXJ12585812+2735409	13.16±0.06	12.06±0.04	1.37±0.22	2.12±0.10	15.76±0.35	15.53±0.11	2.166±0.011
2MASXJ12573284+2736368	11.65±0.01	10.62±0.01	3.47±0.06	3.76±0.09	16.27±0.04	15.33±0.05	2.379±0.008
2MASXJ13020106+2739109	13.41±0.03	12.70±0.07	4.01±0.19	3.02±0.24	18.32±0.11	16.91±0.19	1.805±0.026
2MASXJ13015375+2737277	10.90±0.01	10.05±0.01	6.76±0.20	5.49±0.07	16.94±0.06	15.54±0.03	2.423±0.008
2MASXJ12591030+2737119	13.28±0.04	12.34±0.05	2.76±0.18	2.75±0.25	17.40±0.15	16.38±0.20	2.078±0.014
2MASXJ12571682+2737068	13.51±0.06	12.48±0.05	1.12±0.28	1.18±0.33	15.65±0.55	14.64±0.61	2.208±0.009
2MASXJ12594713+2742372	12.05±0.05	11.14±0.02	4.04±0.27	3.66±0.04	16.97±0.15	15.74±0.03	2.130±0.010
2MASXJ12584742+2740288	11.97±0.01	11.07±0.02	7.20±0.15	6.77±0.11	18.14±0.05	17.00±0.04	2.273±0.009
2MASXJ12583157+2740247	13.94±0.06	12.90±0.07	1.27±0.15	1.80±0.15	16.37±0.26	15.99±0.20	2.104±0.012
2MASXJ12563420+2741150	14.28±0.07	13.82±0.21	3.54±0.37	2.09±0.53	18.93±0.24	17.24±0.59	1.798±0.029
2MASXJ13000626+2746332	12.97±0.03	11.98±0.04	4.29±0.25	4.21±0.15	18.04±0.13	16.94±0.09	2.061±0.013
2MASXJ12592491+2744198	13.15±0.04	12.27±0.04	1.65±0.76	1.96±0.13	16.15±1.00	15.58±0.15	2.159±0.012
2MASXJ12591348+2746289	12.65±0.02	11.90±0.03	4.39±0.20	3.41±0.11	17.77±0.10	16.38±0.08	2.071±0.014
2MASXJ12590821+2747029	12.12±0.03	11.13±0.02	3.38±0.09	3.45±0.08	16.67±0.07	15.63±0.06	2.314±0.009
2MASXJ12590745+2746039	12.90±0.05	11.98±0.04	2.13±0.10	2.25±0.06	16.45±0.11	15.57±0.07	2.223±0.010
2MASXJ12585766+2747079	13.69±0.05	13.12±0.09	4.24±0.40	3.41±0.37	18.73±0.21	17.60±0.25	1.582±0.055
2MASXJ12585208+2747059	12.43±0.02	11.65±0.03	4.01±0.24	3.34±0.09	17.37±0.13	16.11±0.06	2.175±0.011
2MASXJ12581922+2745437	14.28±0.08	13.48±0.13	2.41±0.12	1.86±0.40	18.12±0.13	16.68±0.49	1.872±0.031
2MASXJ12574616+2745254	12.75±0.02	12.15±0.04	7.93±0.20	5.02±0.34	19.17±0.06	17.49±0.15	1.696±0.042
2MASXJ13011761+2748321	11.91±0.02	10.88±0.01	3.38±0.03	3.69±0.03	16.46±0.02	15.53±0.02	2.274±0.009
2MASXJ13003334+2749266	14.46±0.11	13.53±0.12	3.25±0.41	3.44±0.31	18.91±0.30	18.00±0.23	1.625±0.060
2MASXJ13000551+2748272	12.55±0.02	11.89±0.03	4.75±0.16	3.30±0.10	17.84±0.08	16.31±0.07	2.067±0.013
2MASXJ12595489+2747453	14.40±0.11	13.74±0.13	2.07±0.35	1.47±0.35	17.87±0.39	16.36±0.53	1.658±0.041
2MASXJ12593697+2749327	14.50±0.12	13.62±0.15	1.08±0.10	1.36±0.41	16.57±0.23	16.13±0.68	1.927±0.023
2MASXJ12592936+2751008	12.35±0.03	11.41±0.02	2.87±0.26	2.29±0.02	16.55±0.20	15.02±0.03	2.387±0.009
2MASXJ12580349+2748535	12.85±0.04	12.03±0.04	2.44±0.10	2.03±0.14	16.69±0.10	15.37±0.15	2.216±0.009
2MASXJ12574728+2749594	12.89±0.03	12.11±0.04	2.25±0.15	2.16±0.05	16.57±0.14	15.63±0.06	2.118±0.012
2MASXJ12571778+2748388	13.89±0.07	12.86±0.08	2.98±0.25	3.62±0.25	18.16±0.19	17.46±0.17	1.710±0.038

Table 4 continued ...

Identification	Total magnitude		Effective radius		Mean eff. surf. brightness		$\log \sigma$
	J	K_s	J	K_s	J	K_s	
(1)	(2)	(3)	(4)	(5)	(6)	(7)	(8)
2MASXJ13025272+2751593	12.25±0.02	11.29±0.02	3.10±0.35	2.82±0.10	16.59±0.25	15.33±0.08	2.186±0.009
2MASXJ13015023+2753367	12.52±0.02	11.67±0.03	3.09±0.08	2.64±0.02	16.88±0.06	15.58±0.03	2.290±0.010
2MASXJ12594610+2751257	13.22±0.04	12.08±0.04	1.97±0.04	2.48±0.08	16.58±0.06	15.84±0.08	2.090±0.011
2MASXJ12593789+2754267	12.64±0.03	11.49±0.03	2.36±0.02	2.93±0.11	16.40±0.04	15.61±0.09	2.261±0.009
2MASXJ12592016+2753098	13.41±0.04	12.48±0.05	3.28±0.20	3.12±0.35	17.90±0.14	16.78±0.25	1.831±0.021
2MASXJ12590459+2754389	13.33±0.04	12.73±0.08	2.94±0.14	2.06±0.13	17.58±0.11	16.13±0.16	2.044±0.012
2MASXJ12590791+2751179	12.45±0.03	11.46±0.03	3.11±0.20	2.78±0.11	16.82±0.15	15.51±0.09	2.258±0.009
2MASXJ12575059+2752454	13.49±0.03	12.50±0.05	2.82±0.65	3.03±0.10	17.65±0.50	16.72±0.08	2.013±0.017
2MASXJ12572169+2752498	13.89±0.06	12.92±0.09	2.38±0.06	2.44±0.30	17.67±0.08	16.66±0.28	1.685±0.037
2MASXJ13004285+2757476	13.25±0.07	12.11±0.04	2.21±0.25	3.05±0.22	16.85±0.25	16.31±0.17	2.060±0.012
2MASXJ13004737+2755196	13.02±0.03	12.54±0.06	5.33±0.25	3.09±0.20	18.54±0.11	16.76±0.15	1.944±0.016
2MASXJ13003975+2755256	12.29±0.02	11.18±0.02	3.37±0.09	4.40±0.03	16.82±0.06	16.20±0.02	2.240±0.009
2MASXJ13002798+2757216	13.24±0.04	12.26±0.05	2.29±0.06	2.28±0.06	16.94±0.07	15.86±0.08	2.121±0.011
2MASXJ12595670+2755483	13.44±0.04	12.49±0.05	4.16±0.32	3.76±0.33	18.43±0.17	17.16±0.20	2.001±0.016
2MASXJ12594438+2754447	12.30±0.02	11.25±0.02	3.44±0.03	3.74±0.09	16.89±0.02	15.93±0.06	2.207±0.009
2MASXJ12594234+2755287	13.56±0.07	12.53±0.05	1.07±0.21	1.20±0.15	15.62±0.42	14.74±0.27	2.238±0.011
2MASXJ12594423+2757307	13.60±0.05	12.68±0.07	2.99±0.12	3.10±0.25	17.88±0.10	16.95±0.19	1.819±0.025
2MASXJ12593570+2757338	9.81±0.00	8.98±0.00	26.13±0.03	20.02±0.12	18.80±0.00	17.30±0.01	2.426±0.009
2MASXJ12590414+2757329	14.08±0.10	12.98±0.11	1.74±0.31	2.10±0.32	17.18±0.39	16.40±0.35	2.112±0.014
2MASXJ12565310+2755458	13.27±0.09	12.26±0.04	1.21±0.08	1.25±0.01	15.60±0.17	14.59±0.05	2.272±0.009
2MASXJ12562984+2756240	12.81±0.03	11.70±0.03	2.48±0.68	3.47±0.15	16.69±0.60	16.23±0.10	2.266±0.009
2MASXJ13012713+2759566	13.69±0.08	12.60±0.05	0.87±0.15	1.15±0.16	15.29±0.39	14.70±0.31	2.198±0.010
2MASXJ13005445+2800271	11.40±0.01	10.46±0.01	7.55±0.03	6.97±0.18	17.72±0.01	16.54±0.06	2.371±0.009
2MASXJ13003877+2800516	13.03±0.04	11.97±0.03	3.86±0.08	4.58±0.16	17.86±0.06	17.07±0.08	2.026±0.014
2MASXJ13000809+2758372	9.67±0.00	8.51±0.00	14.79±0.15	17.27±0.06	17.43±0.02	16.52±0.01	2.570±0.008
2MASXJ13000643+2800142	12.94±0.03	12.02±0.04	3.25±0.06	3.22±0.23	17.40±0.05	16.37±0.16	2.081±0.013
2MASXJ12594681+2758252	12.70±0.02	11.53±0.02	3.55±0.09	4.60±0.11	17.33±0.06	16.60±0.05	2.116±0.012
2MASXJ12593827+2759137	13.80±0.05	13.11±0.10	3.80±0.27	3.70±0.48	18.60±0.16	17.77±0.30	1.909±0.022
2MASXJ12592657+2759548	14.28±0.10	13.06±0.09	1.77±0.23	2.27±0.13	17.43±0.30	16.66±0.16	1.904±0.018
2MASXJ12592136+2758248	14.44±0.13	13.48±0.14	2.26±0.22	2.53±0.53	18.13±0.24	17.34±0.47	1.713±0.050
2MASXJ12590603+2759479	12.23±0.02	11.30±0.02	4.68±0.25	4.83±0.24	17.48±0.12	16.52±0.11	2.179±0.010
2MASXJ12583023+2800527	11.81±0.01	11.14±0.02	5.87±0.19	3.71±0.03	17.55±0.07	15.80±0.03	2.282±0.009
2MASXJ13025659+2804133	13.00±0.03	12.22±0.05	4.59±0.25	4.45±0.10	18.21±0.12	17.26±0.07	1.753±0.030
2MASXJ13024442+2802434	12.04±0.01	10.98±0.02	5.22±0.08	6.38±0.26	17.55±0.04	16.84±0.09	2.254±0.010
2MASXJ13004867+2805266	11.93±0.02	10.89±0.01	3.28±0.04	3.60±0.02	16.42±0.03	15.48±0.02	2.321±0.008
2MASXJ13002215+2802495	12.68±0.03	11.54±0.03	3.48±0.09	4.56±0.17	17.29±0.06	16.62±0.08	2.087±0.011
2MASXJ13001702+2803502	13.35±0.05	12.35±0.04	2.68±0.26	2.40±0.23	17.40±0.21	16.09±0.21	2.070±0.013
2MASXJ13001475+2802282	12.80±0.03	11.80±0.03	1.91±0.05	2.11±0.03	16.13±0.07	15.27±0.04	2.206±0.010
2MASXJ13001286+2804322	13.20±0.04	12.35±0.05	2.15±0.10	1.85±0.10	16.77±0.11	15.48±0.12	2.075±0.011
2MASXJ13000803+2804422	12.66±0.04	11.57±0.02	1.83±0.04	2.13±0.07	15.88±0.07	15.02±0.08	2.263±0.008
2MASXJ12595601+2802052	12.13±0.02	11.04±0.02	3.99±0.13	4.85±0.15	17.03±0.07	16.25±0.07	2.206±0.010
2MASXJ12593141+2802478	12.70±0.03	11.86±0.04	3.29±0.13	2.88±0.13	17.18±0.09	15.98±0.10	2.108±0.011
2MASXJ12591389+2804349	12.78±0.02	12.11±0.05	6.60±0.11	5.36±0.26	18.77±0.04	17.55±0.12	2.150±0.014
2MASXJ12564585+2803058	14.52±0.09	13.51±0.12	2.70±0.18	2.83±0.48	18.59±0.17	17.59±0.39	1.669±0.048
2MASXJ12563890+2804518	13.94±0.07	13.17±0.11	4.35±0.32	4.55±0.61	19.03±0.17	18.25±0.31	1.625±0.062
2MASXJ13014700+2805417	12.23±0.02	11.11±0.02	2.67±0.02	3.47±0.03	16.28±0.02	15.66±0.02	2.257±0.008
2MASXJ13004459+2806026	13.18±0.04	12.46±0.05	4.14±0.28	2.92±0.20	18.18±0.15	16.61±0.16	1.891±0.017
2MASXJ13003552+2808466	13.04±0.03	11.96±0.03	3.91±0.22	4.56±0.16	17.92±0.13	17.11±0.08	1.885±0.020

Table 4 continued ...

Identification (1)	Total magnitude		Effective radius		Mean eff. surf. brightness		log σ (8)
	J (2)	K_s (3)	J (4)	K_s (5)	J (6)	K_s (7)	
2MASXJ12595511+2807422	13.33±0.05	12.25±0.04	2.32±0.27	2.98±0.23	17.05±0.26	16.42±0.17	2.096±0.014
2MASXJ12590392+2807249	11.37±0.01	10.35±0.01	4.77±0.13	4.90±0.12	16.65±0.06	15.59±0.05	2.422±0.008
2MASXJ12585341+2807339	13.39±0.06	12.52±0.05	2.34±0.11	2.10±0.09	17.14±0.12	15.95±0.11	2.062±0.013
2MASXJ12583636+2806497	11.98±0.01	11.25±0.02	5.19±0.09	3.53±0.07	17.46±0.04	15.80±0.04	2.239±0.009
2MASXJ12574670+2808264	14.04±0.07	13.41±0.14	4.16±0.45	3.76±0.83	19.04±0.24	18.11±0.50	1.607±0.066
2MASXJ13021025+2811309	13.90±0.07	13.05±0.11	3.95±0.39	3.01±0.43	18.80±0.23	17.30±0.33	1.834±0.025
2MASXJ13012280+2811456	12.97±0.03	12.12±0.04	4.00±0.53	3.35±0.22	17.88±0.29	16.55±0.15	2.109±0.013
2MASXJ13001795+2812082	11.41±0.01	10.12±0.01	4.26±0.02	6.45±0.13	16.44±0.02	15.95±0.04	2.369±0.008
2MASXJ12592021+2811528	13.99±0.06	12.88±0.05	2.32±0.10	2.94±0.18	17.69±0.11	16.97±0.14	1.949±0.022
2MASXJ12581382+2810576	12.94±0.02	12.13±0.05	6.46±0.11	5.57±0.30	18.89±0.04	17.67±0.12	1.869±0.019
2MASXJ12574866+2810494	12.70±0.03	11.69±0.03	2.72±0.11	2.65±0.22	16.77±0.09	15.62±0.18	2.159±0.011
2MASXJ12572841+2810348	13.18±0.11	11.69±0.03	2.71±0.20	4.54±0.14	17.24±0.19	16.76±0.07	2.021±0.015
2MASXJ12563516+2816318	12.69±0.02	12.03±0.04	4.67±0.24	3.04±0.20	17.93±0.11	16.26±0.15	2.090±0.013
2MASXJ12592611+2817148	14.31±0.08	13.58±0.12	2.02±0.12	1.86±0.35	17.73±0.15	16.72±0.42	1.695±0.039
2MASXJ12584394+2816578	14.49±0.18	13.78±0.17	2.26±0.38	1.49±0.36	18.15±0.41	16.45±0.55	1.629±0.046
2MASXJ12582949+2818047	14.16±0.09	13.29±0.12	2.76±0.25	2.44±0.50	18.28±0.21	17.07±0.46	1.844±0.027
2MASXJ13024079+2822163	12.42±0.02	11.45±0.03	5.40±0.15	5.14±0.24	17.99±0.06	16.81±0.11	1.941±0.020
2MASXJ13021434+2821099	13.50±0.04	12.62±0.08	5.46±0.19	5.40±0.56	19.07±0.09	18.05±0.24	1.855±0.032
2MASXJ13020865+2823139	12.16±0.01	11.01±0.02	4.61±0.11	5.61±0.17	17.37±0.05	16.56±0.07	2.213±0.020
2MASXJ13010904+2821352	13.13±0.03	12.51±0.05	4.88±0.39	2.65±0.39	18.48±0.18	16.44±0.33	1.879±0.018
2MASXJ13005207+2821581	11.82±0.01	10.80±0.01	3.89±0.10	4.27±0.10	16.67±0.06	15.75±0.05	2.240±0.010
2MASXJ13004423+2820146	12.52±0.02	11.78±0.03	3.41±0.03	2.82±0.20	17.08±0.02	15.82±0.16	2.098±0.010
2MASXJ13003074+2820466	11.70±0.01	10.78±0.01	6.63±0.08	6.03±0.15	17.72±0.03	16.53±0.06	2.205±0.009
2MASXJ13023199+2826223	14.07±0.13	13.44±0.16	5.11±0.84	3.70±0.76	19.53±0.38	18.12±0.48	1.776±0.064
2MASXJ12575392+2829594	13.40±0.07	12.46±0.06	1.15±0.28	1.69±0.21	15.60±0.54	15.42±0.28	2.121±0.012
2MASXJ12593568+2833047	13.16±0.05	12.25±0.04	2.07±0.42	2.26±0.11	16.64±0.44	15.82±0.11	2.113±0.012
2MASXJ12565652+2837238	12.75±0.03	11.97±0.03	4.05±0.19	2.95±0.16	17.70±0.11	16.14±0.13	2.036±0.013